論文 / 著書情報
Article / Book Information

Title	Evaluation of seismic residual capacity ratio for reinforced concrete structures
Authors	Alex Shegay, Kota Miura, Kisho Fujita, Yu Tabata, Masaki Maeda, Matsutaro Seki
Citation	Resilient Cities and Structures, Volume 2, Issue 1, pp. 28-45
Pub. date	2023, 3
DOI	https://dx.doi.org/10.1016/j.rcns.2023.02.004

Resilient Cities and Structures 2 (2023) 28–45

Contents lists available at ScienceDirect

Resilient Cities and Structures

journal homepage: www.elsevier.com/locate/rcns

Full Length Article

Evaluation of seismic residual capacity ratio for reinforced concrete structures

Alex V. Shegay[a,*], Kota Miura[b], Kisho Fujita[c], Yu Tabata[d], Masaki Maeda[e], Matsutaro Seki[f]

[a] Tokyo Institute of Technology, 4259 Nagatsuta, Midori-ku, Yokohama, Japan
[b] Obayashi Technical Research Institute, 4-640 Shimokiyoto, Kiyose, Japan
[c] Obayashi Corporation, 2-15-2 Konan, Minato-ku Tokyo, Japan
[d] Kume Sekkei Co.Ltd, 2-1-2 Shiomi, Koto-ku Tokyo, Japan
[e] Tohoku University, 1220, 6-6-11 Aramaki Aoba, Aoba-ku, Sendai, Japan
[f] Building Research Institute, Tsukuba-shi, Tachihara 1, Japan

ARTICLE INFO

Keywords:
Seismic residual capacity ratio
Reinforced concrete
Earthquake engineering
Shake-table test
Damage evaluation
Numerical modeling

ABSTRACT

Use of indices that quantify the seismic residual capacity of buildings damaged in earthquakes is one way to draw judgements on the building's safety and possibility of future use. In Japanese damage assessment guidelines, several approximate calculation methods exist to evaluate the residual capacity of buildings based on visually observed damage and simplifying assumptions on the nature of the building's response mechanism and member capacities. While these methods provide a useful residual capacity ratio that enables a 'relative' comparison between buildings, the exact relationship to a physically meaningful residual capacity is unclear. The aim of this study is to benchmark the 'approximations' of residual capacity. To do so, a shake-table test was conducted on a $\frac{1}{4}$ scale 4-storey RC structure and a residual capacity evaluation was undertaken based on observed damage states. With the help of a numerical model, a benchmark residual capacity at each of the damage states is determined and compared to the approximate residual capacity calculation results via guidelines. It was found that approximate methods are generally accurate prior to yield but can become overly conservative post-yield. Simplifying assumptions of equal member deformation capacity used in the residual capacity ratio calculation was found to be suitable given constraints of rapid field evaluations.

1. Introduction

Damage assessments of buildings are critical following strong earthquakes to determine whether they are structurally safe for immediate reoccupation or are in need of repairs. The 'seismic residual capacity ratio' (hereinafter 'residual capacity ratio') of the structure, that is, the seismic capacity of the damaged structure as a fraction of its undamaged capacity, is a useful metric for quantifying the extent of structural damage and provide an insight into the building's performance in future earthquakes. Existing experimental studies on seismic residual capacity of reinforced concrete (RC) structures is generally limited to component level studies (e.g., columns [1,2], beams [3,4] walls [5]). In such experimental programs, components are tested to quantify the effect of varying initial damage conditions on the component's overall performance. Based on the results of such experimental programs, several studies have proposed plastic hinge modification factors to be used in lumped plasticity models to account for changes in component stiffness, energy dissipation, deformation capacity and strength characteristics due to damage [6–10]. FEMA 306 [11] provides a framework for using such data in pushover and time history analysis methods to estimate the performance of damaged structures. In field damage assessments, challenges of time constraints, limited personnel, and large building stock means that detailed assessments involving numerical modeling are usually not realistic. In such scenarios, a rapid assessment method of residual capacity ratio is desired.

Though recent studies have proposed rapid evaluation methods of residual capacity ratio via acceleration response data [12,13], common practice for rapid damage assessment methodologies around the world still predominantly relies on judgements made via visual observation (e.g., Japan [14], New Zealand [15], USA [16], Taiwan [17], Italy [18]). The outcome of these assessments is usually in the form of a placard to indicate if the building is safe for reoccupation; requires caution and/or minor repair prior to reoccupation, or is unsafe to enter. Among these, the 'Guidelines for Post-earthquake Damage Evaluation and Rehabilitation' published by the Japanese Building Disaster Prevention Association (hereinafter, 'JBDPA Guidelines') [14] is the only document to quantify

* Corresponding author.
E-mail address: shegay.a.aa@m.titech.ac.jp (A.V. Shegay).

https://doi.org/10.1016/j.rcns.2023.02.004
Received 11 December 2022; Received in revised form 6 February 2023; Accepted 7 February 2023

a residual capacity ratio for the entire building. The JBDPA Guidelines provide several approximate calculation methods of residual capacity ratio (detailed in the following sections) that do not involve numerical analysis. These assessment procedures have been extensively used in Japan to rate damaged buildings in previous major earthquakes [19]; however, have been generally only useful for relative performance comparisons. In other words, the relationship between the residual capacity ratio computed through the JBDPA Guidelines and the expected future performance of the structure has not been verified experimentally nor through real life case studies. Hence, the reliability of these assessment methods in predicting future earthquake performance is unclear. The objective of this study is to resolve some of this uncertainty by quantifying the level of accuracy in the residual capacity ratio calculation methods in the JBDPA Guidelines. The comparison will be done with respect to a subject structure tested on a shake-table as part of this study. A method to determine the residual capacity ratio from the experimental data will be demonstrated with the aid of a numerical model. Residual capacity ratio will be evaluated at the structure's global level, rather than at the local component-level common in previous studies.

This paper begins by first defining the residual capacity ratio and introducing the methods available to estimate it in the JBDPA Guidelines. The key underlying assumptions used in these estimate methods are also identified. An experimental program designed to test some of these assumptions is then introduced. Next, using a numerical model calibrated to the experimental results the experimental residual capacity ratio is computed and compared to that calculated using the JBDPA Guidelines.

2. Residual capacity ratio assessment using the JBDPA Guidelines

In Japan, earthquake damage in RC buildings is quantified by an overall residual capacity ratio. In the JBDPA Guidelines, the magnitude of the residual capacity ratio is used to make repair/demolition decisions for damaged buildings, with previous earthquake reconnaissance data suggesting a value of ~60% as a potential limit for building repairability [20,21]. Details of the decision matrix are provided in Appendix A. A rational physical interpretation of the residual capacity ratio has been offered by Maeda et al. [22] as the ratio of the intensity of ground motion required for a damaged building to reach its ultimate limit state, to the corresponding intensity required for a building in its undamaged state. In this study, this definition is adopted as the benchmark residual capacity ratio of a building, R_b, and is determined analytically because it is impractical to do so through pure experimentation. The ground motion intensity measure adopted in this study is the spectral acceleration at the first natural period of the undamaged building, ${}_uT_1$ [23]. Therefore, defining the ultimate limit state spectral acceleration for the undamaged building as ${}_uS_a$, and for the damaged building as ${}_dS_a$, the benchmark residual capacity ratio can be expressed by Eq. (1) as follows:

$$R_b = \frac{{}_dS_a}{{}_uS_a} \tag{1}$$

Conceptually, the above definition is a measure of the energy dissipation capacity of a building in its damaged state relative to that in its undamaged state. The advantage of this definition is that it implicitly considers changes in system-level characteristics (e.g., load redistribution, natural period shifts, higher mode effects) that cannot be considered in the aforementioned component-level studies. Similarly, the JBDPA Guidelines provide several methods to compute the residual capacity ratio through the concept of energy dissipation capacity, albeit via simplified methods (full details of which can be found in [20,24]). In this paper, the two JBDPA methods most commonly used in practice: the 'internal energy method' and the 'simplified internal energy method' will be compared to R_b with respect to the structure tested in this study. A description of these methods is provided next.

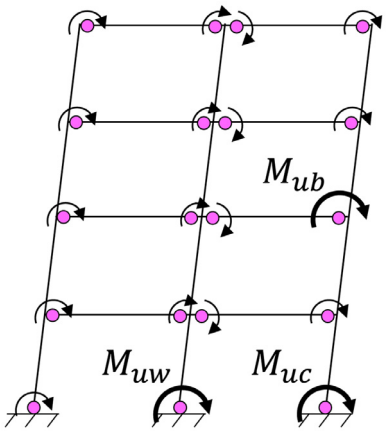

Fig. 1. Energy dissipation locations in a typical structure exhibiting a strong column-weak beam yielding mechanism.

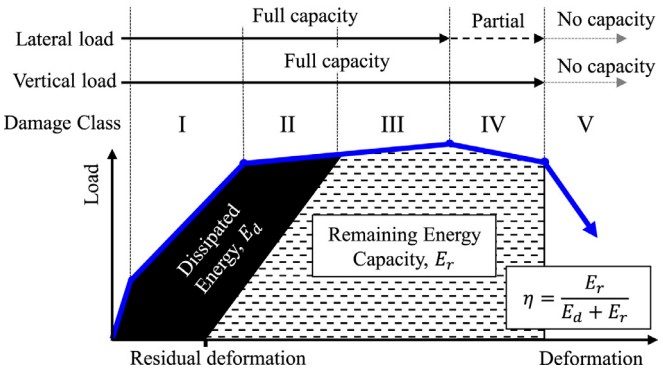

Fig. 2. Visual representation of damage states and damage reduction η-factor [14,20].

2.1. The internal energy method

In this method, the total structural seismic capacity is quantified as its total energy dissipation capacity. From this definition, it follows that the residual capacity ratio, R_{IE}, is simply the remaining energy dissipation capacity throughout a damaged structure as a fraction of the total energy capacity available in the undamaged state. For buildings expected to exhibit a strong column-weak beam yielding mechanism, such as that shown in Fig. 1, energy dissipation can be assumed to occur only at the plastic hinge locations, so the process of determining total energy dissipation capacity becomes an exercise of summing the individual energy dissipation capacities of each hinge. The reduction in energy dissipation capacity of each plastic hinge resulting from structural damage is quantified by a reduction factor, η. A theoretical interpretation of the η-factor is shown in Fig. 2 and is the remaining energy dissipation capacity in a plastic hinge after damage as a fraction of the total initial energy dissipation capacity (i.e., dissipated energy plus remaining energy dissipation capacity). The η-factors are available in the JBDPA Guidelines for various member types and depend on the visually assessed Damage Level. Damage Level definitions and η-factors from the JBDPA Guidelines are reproduced in Tables 1 and 2, respectively [14,20]. An interpretation of the Damage Levels for flexural members relative to their backbone characteristics is shown in Fig. 2. Based on the above definitions, the residual capacity ratio can be expressed as follows:

$$R_{IE} = \frac{\sum_{i=1}^{N_w} \eta_{w,i} M_{uw,i} \theta_{uw,i} + \sum_{i=1}^{N_b} \eta_{b,i} M_{ub,i} \theta_{ub,i} + \sum_{i=1}^{N_c} \eta_{c,i} M_{uc,i} \theta_{uc,i}}{\sum_{i=1}^{N_w} M_{uw,i} \theta_{uw,i} + \sum_{i=1}^{N_b} M_{ub,i} \theta_{ub,i} + \sum_{i=1}^{N_c} M_{uc,i} \theta_{uc,i}} \tag{2}$$

Table 1
Definition of damage levels of structural members [14,20].

Damage Level	Observed damage in structural members
I	Sparse, fine cracks can be observed (<0.2 mm). No reinforcement yielding expected.
II	Clearly visible cracks (0.2–1 mm) exist.
III	Wide cracks (1–2 mm) are present. Plastic hinging mechanisms begin to form. Some spalling of cover concrete is observed but concrete core is in-tact.
IV	Many wide cracks are observed. Compression damage resulting in concrete spalling and exposed reinforcement. Lateral strength degradation may occur, but vertical load is still fully carried by walls and columns.
V	Buckling (and in some cases fracture) of reinforcement, crushing of concrete and vertical deformation of columns and/or shear walls observed. Settlement and inclination of structure are characteristic.

Table 2
Damage reduction η-factors for damaged structural elements [14,20].

Damage Level	RC Column			RC Wall		RC Beam	
	Shear	Shear-flexure	Flexure	Shear	Flexure	Shear	Flexure
I	0.95	0.95	0.95	0.95	0.95	0.95	0.95
II	0.60	0.70	0.75	0.60	0.70	0.70	0.75
III	0.30	0.40	0.50	0.30	0.40	0.40	0.50
IV	0	0.10	0.20	0	0.10	0.10	0.20
V	0	0	0	0	0	0	0

Where M_u, θ_u and η are the member ultimate moment capacity, ultimate deformation capacity and damage reduction η-factor, respectively. N is the total number of hinges for each member type in the structure, and the subscripts 'w', 'b' and 'c' in all terms correspond to wall, beam, and column members, respectively.

2.2. The simplified internal energy method

For buildings with no significant horizontal or vertical irregularities and comprised predominantly of flexural members (e.g., RC moment frames), the JBDPA Guidelines stipulate that an equal ultimate deformation capacity can be assumed for all member hinge types (i.e., $\theta_{uw} = \theta_{ub} = \theta_{uc}$). With this assumption, Eq. (2) can be conveniently reduced to an expression based only on hinge strengths, as shown in Eq. (3). As with the internal energy method in Eqs. (2), (3) is conceptually also a measure of residual energy dissipation capacity.

$$R_{SIE} = \frac{\sum_{i=1}^{N_w} \eta_{w,i} M_{uw,i} + \sum_{i=1}^{N_b} \eta_{b,i} M_{ub,i} + \sum_{i=1}^{N_c} \eta_{c,i} M_{uc,i}}{\sum_{i=1}^{N_w} M_{uw,i} + \sum_{i=1}^{N_b} M_{ub,i} + \sum_{i=1}^{N_c} M_{uc,i}} \quad (3)$$

Where R_{SIE} is the residual capacity ratio based on the simplified internal energy method, and all other terms are as previously defined. The above simplification will produce a more conservative residual capacity ratio compared to R_{IE} in cases where deformation capacity is higher and damage state (quantified via η-factor) is lower in frame members compared to wall members (both conditions are typical for RC structures). The accuracy of the two residual capacity ratio assessment methods introduced above will be assessed against R_b obtained from an experimental case study described next.

3. Experimental program

To obtain experimental data for the progressive loss of seismic capacity in RC structures, a 4-storey $\frac{1}{4}$ scale RC structure was designed and dynamically tested via shake-table over gradually increasing ground motion intensity. The dimensions and an image of the experimental structure are shown in Fig. 3. The member cross-section details are summarized in Table 3. The structure was designed as a new office building located in Tokyo on Type 2 soil [25], using current Architectural Institute of Japan structural calculation standards (hereinafter 'AIJ standards') [26,27]. To test the suitability of the 'equal deformation capacity' assumption used in the calculation of R_{SIE}, the experimental structure was designed as a dual wall-frame system. The degree of interaction

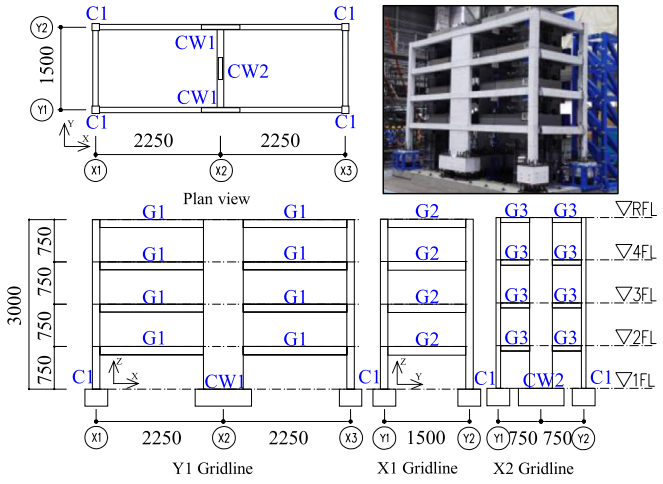

Fig. 3. Dimensions of experimental structure (units: mm).

between the wall and frame was varied in the structure's X-direction (walls designed to carry ~60% of the total base shear) and Y-direction (walls designed to carry ~30% of the total base shear). To account for discrepancy in mass arising as a result of scaling down of the structure, additional mass was added to each story. The total mass of the inner stories and on the roof was 7950 kg and 7640 kg, respectively (3150 kg added per floor). An inter-story drift ratio limit of 0.5% was used for serviceability limit state design [26]. For ultimate limit state design (known as 'safety limit state' in the AIJ standard [26]), no fixed inter-story drift ratio limit is prescribed. Instead, the inter-story drift at which any one member reaches its deformation capacity (calculated using procedures in the AIJ standards [26]) first is set as the building's safety limit state. In the X and Y-directions of the test structure, the RC walls (CW1 and CW2, respectively) reach their ultimate deformation capacity first at approximately 2% inter-story drift ratio. Thus, the safety limit of the structure was set to be 2% in both the X and Y-directions.

3.1. Structural member details

Sectional strengths of members in the test structure are listed in Table 3 and the measured material properties are summarized in Tables 4 and 5 for concrete and reinforcement, respectively. Section moment and probable shear capacity were determined using measured material properties and according to equations in the AIJ standards. The design column to beam moment capacity ratio was 1.15 or higher for all hinges when considering the slab effective width determined via the AIJ standard (see Appendix B for details). In reality, this ratio was as low as 0.5 due to the effective slab width being likely equal to the full slab width (as described in a later section). The beam strengths listed in Table 3 are reported for a full effective slab width assumption. For in-plane walls, the flexural capacity, M_u, was determined from sectional analysis at the point when a third of all the longitudinal reinforcement

Table 3
Details of member sections comprising the test structure (units: mm, kN, kNm).

Member	Column		Wall				Beam						Slab
Name	C1		CW1		CW2		G1		G2		G3		
Section			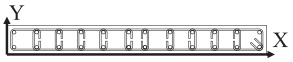		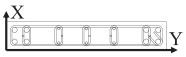		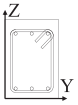		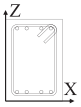		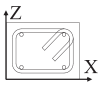		
Size (mm)	130 × 130		80 × 700		70 × 400		100 × 140		100 × 150		120 × 90		70
Main bar	6-D10		24-D10		8-D13 + 6-D6		6-D6		8-D6		4-D6		D4@80 (X-dir.)
Hoop/tie	D4@60		D4@60		D4@100 (cross-ties D4@50)		D4@60		D4@60		D6@30		D4@60 (Y-dir.)
	X	Y	X	Y	X	Y	+ve[a]	−ve	+ve	−ve	+ve	−ve	
M_u, kNm	7.0	9.5	185.0	21.2	10.6	89.0	4.4	10.0	6.4	18.3	1.7	10.7	
V_u, kN	43.4	59.5	325.0	90.0	39.9[b]	117	44.1	44.1	48.6	48.6	27.7	27.7	
θ_u, rad	0.041	0.041	0.021	0.043	0.043	0.022	0.044	0.050	0.039	0.047	0.039	0.047	

[a] +ve refers to positive bending, i.e., top fiber in compression, and -ve refers to negative bending, i.e., top fiber in tension.
[b] Calculated using the 'Arakawa' equation shown in Appendix B as truss-arch method did not provide a valid output.

Table 4
Measured properties of concrete used in the structure.

Grade	Ultimate compressive stress, MPa	Strain at ultimate compressive stress, με	Young's modulus, MPa
Fc30 (early strength)	53.1	2700	2.97×10^4

yields. The ultimate deformation capacities, θ_u, of the members are also summarized in Table 3 and were calculated using [26] as the point at which the shear capacity (a function of deformation) would reduce to match flexural capacity. This definition of ultimate deformation capacity outputted negative values for the G3 beam and out-of-plane bending of the CW2 wall as their flexural capacity exceeded the shear capacity. As a shear failure was deemed unrealistic in both cases, the ultimate deformation capacity for G3 and CW2 was assumed equal to G2 and out-of-plane CW1 values, respectively. The reader is referred to Appendix B for details of the equations used in the strength and deformation capacity calculations.

3.2. Input ground motion characteristics

The structure was subjected to an artificial ground motion pair shown in Fig. 4. The phase of the ground motion corresponded to that recorded at the 'JMA Kobe' observation site during the 1995 Kobe earthquake. The North-South phase record was used in the test structure's X-direction excitation and the East-West phase record was used in the Y-direction. As shown in Fig. 5, the ground motions were tailored in the frequency domain to produce acceleration response spectrums that closely resemble the Japan Building Standard Law (JBSL) design spectrum for a Level 2 'Extremely Rare' event and corresponding to Type 2 soil class [25]. Time of the input record was downscaled by a factor of two to account for the $\frac{1}{4}$ scale of the structure. The structure was subjected to the same orthogonal ground motion pair over a series of nine excitations (hereinafter referred to as 'Runs'). The magnitudes of each Run are summarized in Table 6, and are expressed as a percentage of the Level 2 design earthquake. The excitation magnitude for each Run was decided by targeting a desired overall damage state of the structure:

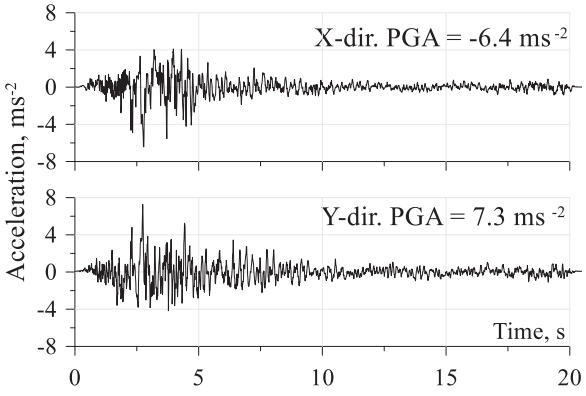

Fig. 4. Artificial acceleration time history records used in the X-direction and Y-direction of the test structure.

Runs 1–3 were intended to excite the structure in the pre-yielding range; Runs 4–5 targeted achieving the maximum strength response and induce failure in the structural walls; Runs 6–8 were intended to increase the deformation demands in order to quantify the residual capacity after the localized wall failures and Run 9 was intended to induce severe damage in all components without causing collapse. The Y-direction loading was terminated following Run 7 due to excessive residual inter-story drift in this direction. An initial white noise test of the structure indicated that the natural period in the undamaged state was ${}_uT_{1,X} = 0.13$ s and ${}_uT_{1,Y} = 0.17$ s in the X and Y-directions, respectively.

3.3. Instrumentation

The main instrumentation plan is shown in Fig. 6. Inter-story displacements were measured via laser transducers attached between the floors of each story (except for the first story, which was measured from an outside reference frame). Beam, column, and wall plastic hinge rotations were measured via displacement transducers at the selected locations shown in Fig. 6. Tri-axial load cells (calibrated uni-axially) were placed under each foundation. Accelerometers were placed on each floor

Table 5
Measured properties of reinforcement used in the structure.

Diameter	Grade	Yield stress, MPa	Ultimate elongation, %	Ultimate stress, MPa	Young's modulus, MPa
4	SD295A	402	No data	533	1.90×10^5
6	SD345	419	24.1	613	1.97×10^5
10	SD345	339	27.9	562	1.93×10^5
13	SD390	407	19.2	602	1.95×10^5

Table 6
Key test structure response characteristics following each Run.

Run	X-direction			Y-direction			Salient damage characteristics
	Magnitude	Δ_{max}, %	V_{max}, kN	Magnitude	Δ_{max}, %	V_{max}, kN	
1	20%	0.07 (2)[a]	51.2	20%	0.07 (2)	48.6	Cracking of structural members.
2	80%	0.31 (2)	167.0	60%	0.22 (1)	128.0	Increasing cracking in members.
3	160%	0.65 (2)	292.4	100%	0.48 (2)	195.1	Column and wall edge longitudinal reinforcement yielding at base.
4	240%	1.36 (3)	402.9	150%	1.30 (2)	290.2	Beam longitudinal reinforcement yields in all stories. Strong column-weak beam yielding mechanism formed in both directions.
5	260%	2.92 (2)	437.8	170%	3.09 (2)	292.2	Concrete cover spalling of first floor X3-Y1 column and CW1 wall end regions. Wide diagonal shear crack in CW2 at 1st and 2nd stories leading to strength degradation. Minor spalling in several G1 and G2 beam hinges.
6	130%	2.20 (2)	290.1	100%	3.05 (1)	248.6	No detailed damage observation conducted.
7	220%	3.51 (2)	406.7	120%	3.94 (1)	243.1	No detailed damage observation conducted.
8	220%	3.99 (2)	427.8	0%	–	–	No detailed damage observation conducted.
9	260%	5.60 (2)	444.2	0%	–	–	Increased concrete spalling at G1 G2 and G3 beam ends. Concrete core crushing and bar buckling in CW1 walls.

[a] () indicates the story where the value was observed.

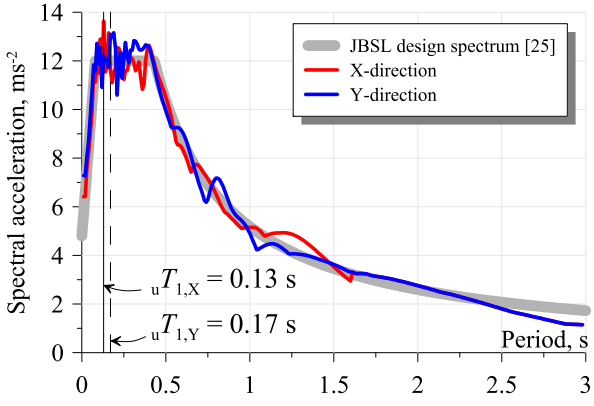

Fig. 5. Acceleration design spectrum [25] plotted with the acceleration response spectrum of the artificial records used in the experiment.

at each corner of the structure (adhered to the slab immediately beside the columns). Accelerometers were also placed at the foundation level to measure the actual acceleration input into the structure. Strain gauges were attached to longitudinal reinforcement at the base of selected columns and walls, and selected beams on each floor to determine when yielding would occur.

3.4. Structural response

Salient damage characteristics, peak inter-story drift ratio, Δ_{max} and peak base shear, V_{max} for each Run are summarized in Table 6. Images of the most severely damaged members following completion of Run 9 are shown in Fig. 7. The base shear – roof drift ratio relationship for the test structure is shown in Fig. 8. Base shear of the structure was determined from the sum of the accelerations of each story multiplied by the respective floor masses, while roof drift ratio was calculated as the sum of the inter-story drifts recorded using lasers divided by the roof height. The damage progression of the structure following each Run is described next.

Flexural cracks appeared in most members following Run 1, and continued to increase in length, width, and number with subsequent Runs. First yielding of longitudinal reinforcement was measured in the base of columns and the X-direction walls during Run 3; however, as can be seen from Fig. 8, no significant nonlinearity was observed in the overall response. Following Run 4, the structure formed an overall yielding mechanism in both the X and Y-directions as can be observed from the increase in hysteretic loop area in Fig. 8. Strain gauge readings of G1, G2 and G3 beam longitudinal reinforcement indicated yielding up the

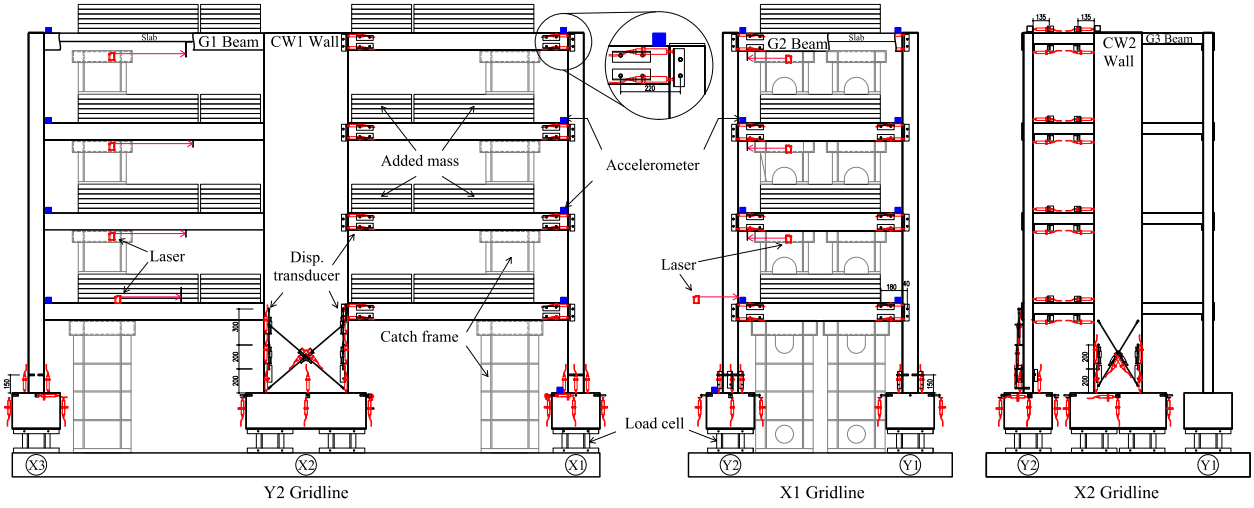

Fig. 6. Instrumentation used on the test structure.

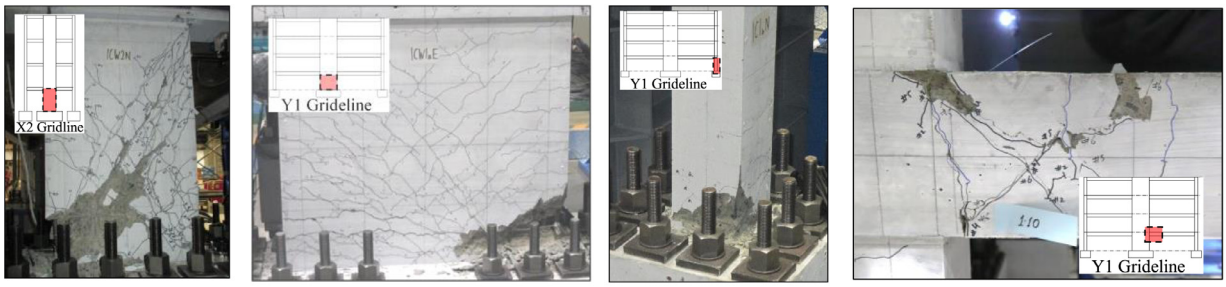

Fig. 7. Most severely damaged structural members after the final excitation (Run 9).

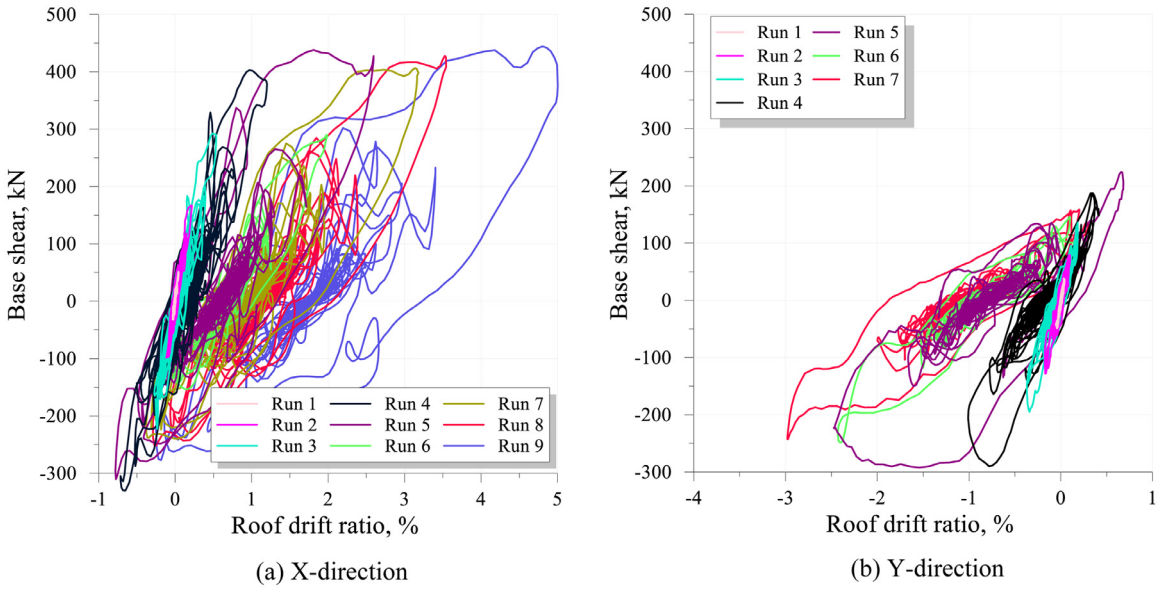

Fig. 8. Base shear-roof drift ratio relationship of the test structure for all Runs.

full height of the structure in both directions, confirming that a strong column-weak beam yielding mechanism had formed. In the Y-direction, yielding of longitudinal and transverse reinforcement of the CW2 wall was also confirmed. During Run 5 maximum inter-story drift ratio increased significantly in both the X-direction (2.92%) and Y-direction (3.09%), compared to the previous Run. Accordingly, damage in the structure increased with spalling observed at the ends of the CW1 walls and the X3 gridline columns. The CW2 wall had undergone a shear failure as was evident by wide diagonal cracking spanning top to bottom of the wall in the first and second stories. Strain gauge readings on the longitudinal reinforcement indicated that CW2 had experienced flexural yield prior to occurrence of the shear failure. Load cells at the bottom of CW2 recorded a base shear demand drop of 21% from the previous peak, accounting partly for the strength reduction seen in the Fig. 8b hysteresis. Inter-story drifts further increased during Run 7, resulting in increased spalling and widening of residual cracks in structural members. The final damage state of the CW2 wall is shown in Fig. 7a. Significant residual drifts in the Y-direction following this run (1.33% in the second story) generated concern for stability, so further excitations in this direction were terminated. In Run 8, the same excitation magnitude of Run 7 (220%) was repeated. Once residual deformation was factored out, the peak roof drift ratio of Run 7 and 8 was found to be only different by 3%. Similar results have been reported in previous studies [28–30], suggesting damage sustained from the initial excitation does not lead to appreciable increases in the peak structural response if that same excitation is repeated (provided no strength degradation occurs). However, as demonstrated by Run 6 in the X-direction (also in [29]), damage incurred from previous excitations will lead to higher peak deformation demands at smaller excitations (relative to the initial excitation causing the damage) compared to loading from an undamaged state. This could be of concern for serviceability requirements if no repair measures are taken to restore the structural stiffness. Finally, during Run 9 the CW1 walls experienced flexural failure characterized by crushing of wall end region concrete and buckling of the first two rows of longitudinal reinforcement, as shown in Fig. 7b. The most damaged beam and column plastic hinges are shown in Fig. 7; no clear longitudinal reinforcement buckling was observed. Measurements during the final run showed that the maximum plastic hinge rotation experienced by the beams G1 G2 and G3 were 4.9%, 2.3% and 4.5%, respectively. The high rotation demand for G3 justified the assumption made for its ultimate deformation capacity in Table 3. At the conclusion of the test maximum inter-story residual drift ratios of 2.10% and 1.33% were recorded in the second story in the X and Y-direction, respectively. The rest of this manuscript will focus on progression of damage and residual capacity evaluation of the structure. Detailed analysis of the structural response can be found in a separate publication [31].

3.5. Safety limit state evaluation

In the Japanese design standards, the building safety limit state is determined as the drift ratio corresponding to failure of any one structural member [25]. While this definition may be appropriate for pure frame or wall structures (as member deformation capacities are approx-

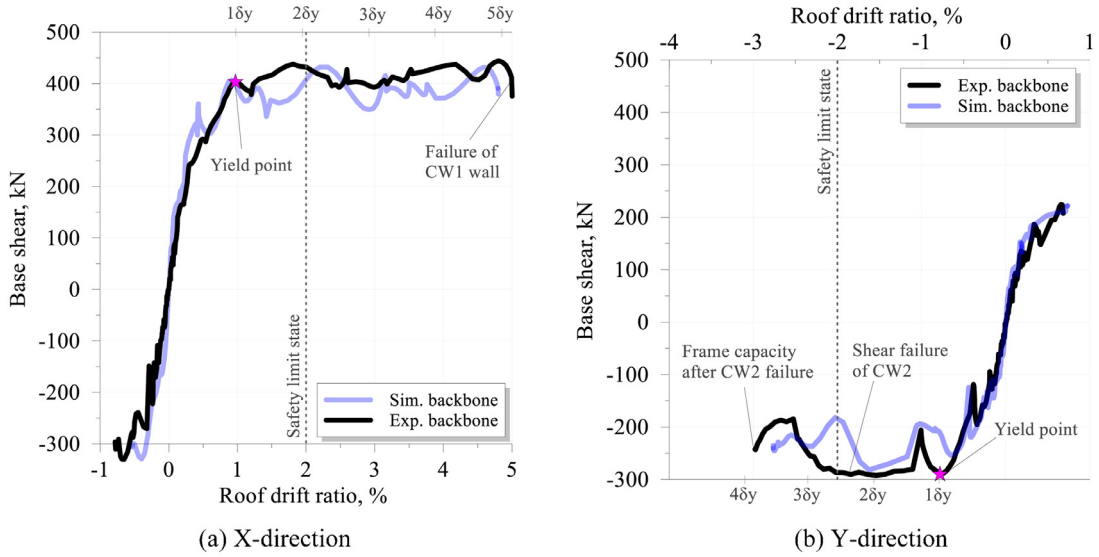

Fig. 9. Base shear-roof drift ratio backbone responses of the test structure.

imately equal), it may not be suitable for dual wall-frame structures. In this section the suitability of the safety limit state definition is investigated by examining the observed structural ductility and member failure progression of the test structure. The backbones of the base shear-roof drift response for the X and Y-directions are shown in Figs. 9a and 9b, respectively. The yield points (determined as the roof drift ratio, δ_y, at which all hinge locations experience reinforcement yielding), structural safety limit state (established earlier in the manuscript to be 2%) and the points corresponding to wall failure are annotated on the backbones for each direction. Though the 2% limit strictly corresponds to a maximum inter-story drift ratio, it is used here for roof drift ratio, given the two were almost equal. In the X-direction, where the CW1 walls exhibited a flexure-governed response, the safety limit state is considerably lower compared to the observed 5% ($>5\delta_y$) drift ratio at which structural strength degradation initiated. Since the safety limit state is governed by the deformation capacity of the wall, these results highlight the importance of accurately calculating the wall deformation capacity in dual structures and the present high level of conservativeness in the AIJ standard to do so for flexural walls. Comparatively, in the Y-direction, where the CW2 wall exhibited a shear-governed response, the safety limit state definition correctly corresponds to the initiation of strength degradation because wall deformation capacity calculation was accurate. However, the safety limit state definition in the Y-direction does not seem to be representative of a concern for safety as the frame possessed large ductility capacity beyond the failure of the wall. Considering that frame members did not fail, the ductility capacity of the structure appears to be at least $4\delta_y$ from Fig. 9b, which is higher than the safety limit state ($\sim 2.5\delta_y$). Therefore, for dual structures, the current definition of safety limit state (being the criterion that any one member fails) by itself is insufficient to arrive at a representative evaluation of the building's safety limit. The contribution of the frame and wall to the overall structural strength (for example, as in [32]), as well as establishing a permissible reduction in strength are also necessary considerations.

3.6. Damage assessment using the JBDPA Guidelines

With the exception of Runs 7 and 8, a detailed visual damage assessment of the structure in accordance with the JBDPA Guidelines was undertaken following each Run. Plastic hinge regions of each structural member were classified as one of the five damage levels listed in Table 1. Damage of all plastic hinges following Runs 4, 5 and 9 are shown in Fig. 10 (Runs 1–3 resulted in scattered damage not exceeding Damage Level I for all members, and is thus not shown for brevity). As can be observed from Fig. 10, in both directions a strong column-weak beam yielding mechanism was formed as intended. The exception of some hinges forming in the column of the 4th story (e.g., Run 9, X3 gridline) is due to the aforementioned stronger than anticipated floor slab contribution to the beam strength. Since damage was observed to concentrate in the plastic hinge regions of the structure, calculation of total energy dissipation capacity as the sum of individual plastic hinge energy dissipation capacities was deemed valid. The damage assessment results were subsequently used to evaluate the seismic residual capacity ratio using the approximate calculation methods from the JBDPA Guidelines (Eqs. 2 and 3). The results of this assessment are presented in a later section.

4. Numerical modeling of structure response

The main purpose of this study was to determine a 'benchmark' value for residual capacity ratio from experimental data and compare to the residual capacity ratio approximations calculated via the JBDPA Guidelines. The definition for the 'benchmark' value for residual capacity ratio, R_b, was previously given in Eq. (1). Determining R_b purely through experimental data is impractical as it requires a pristine test structure to determine ${}_uS_a$, as well as one for each damage state at which ${}_dS_a$ is sought. Moreover, determination of ${}_uS_a$ and ${}_dS_a$ is inevitably a trial-and-error process, whereby each unsuccessful 'trial' (i.e., not reaching the ultimate limit state) will further necessitate a pristine test structure. For this reason, determination of R_b was assisted by a numerical model. Unlike previous studies that have taken this approach to estimate R_b [33,34], in this paper a link to physical phenomena is established by first verifying the accuracy of the model against experimental data. Details of this model are described next.

4.1. Model details

A 3-D lumped plasticity model of the structure was developed in a structural analysis software called SNAP [35]. A schematic of the model is shown in Fig. 11a. Elements between the lumped plastic hinges were elastic for axial and shear demands, based on gross section properties. Beam-column and beam-wall joints were modeled with rigid zones as shown in Fig. 11a. The rigid zone extended from the joint node to the face of the connecting member plus a quarter depth of the hinging member (i.e., taking plastic hinge length as half of the member depth). Walls were also modeled as column members (with a horizontal rigid zone at each floor extending half the wall length plus quarter of the depth of

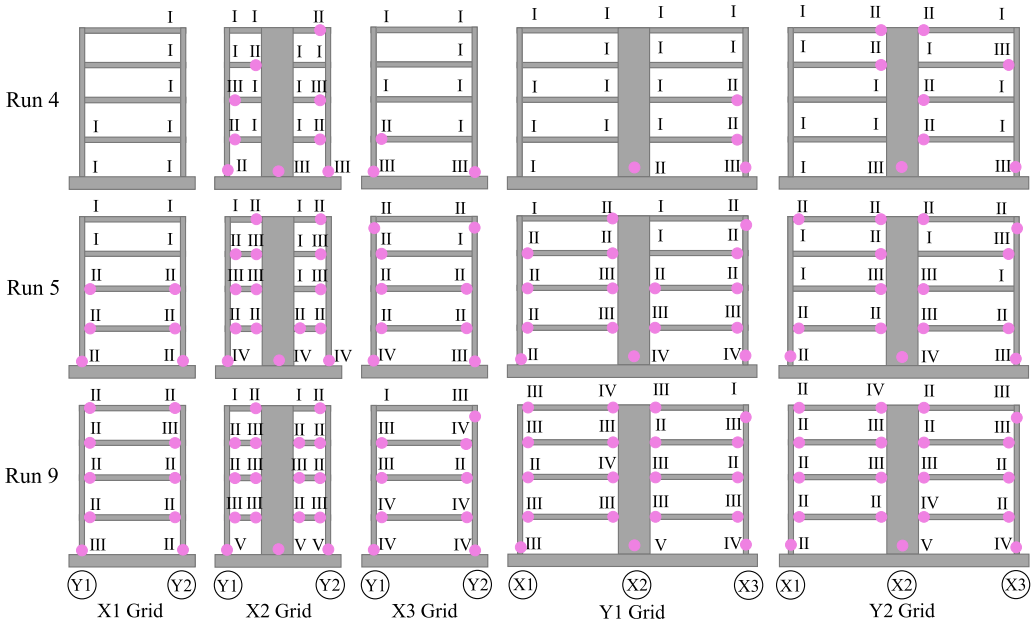

Fig. 10. JBDPA Guidelines visual damage assessment results for Runs 4, 5 and 9 [14].

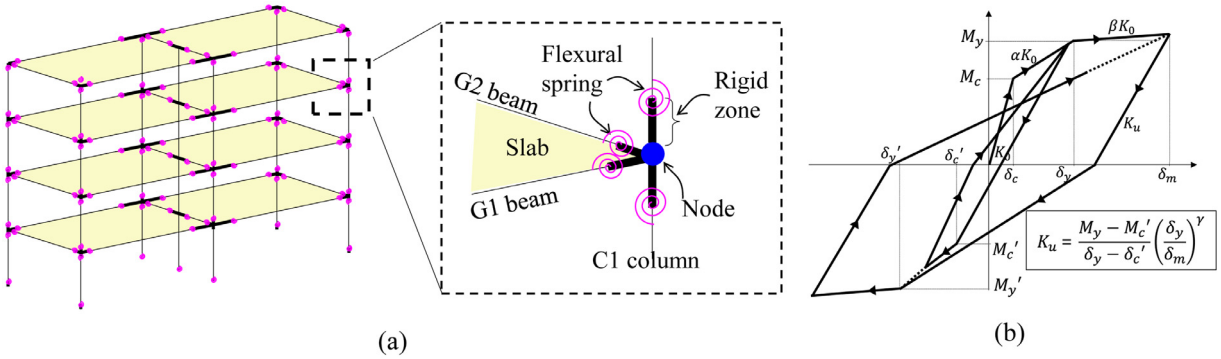

Fig. 11. Modeling approach for the test structure: (**a**) overall line element model details (**b**) Takeda model hysteretic rules adopted for flexural springs [36].

the framing beam at each side of the node), with the critical section set to the bottom of the element.

All plastic hinges in the model were modelled by flexural springs with a trilinear backbone and hysteretic rules obeying the Takeda model [36], as shown in Fig. 11b. In this hysteresis model, the unloading stiffness of the response, K_u, gradually degrades with increasing maximum deformation demands. As shown in the equation in Fig. 11b, the rate of degradation of K_u is controlled via the γ-parameter, which was set to the default value of 0.4 [35,36]. The reloading branches of the models are always oriented towards the historical peak response point; thus, reloading stiffness gradually degrades with increasing maximum deformation demands. Cyclic strength degradation was not simulated in any of the plastic hinges. The absence of cyclic strength degradation in the model is not thought to significantly affect the simulated response given that the number of loading cycles with large reinforcement strain demands (2–4%) in the test structure members is low (at most five cycles, being the largest half-cycles of Runs 4, 5, 7, 8 and 9 in Fig. 8) compared to the typically >10 cycles required to observe the effects of low cycle fatigue [37]. Initial stiffness, K_0, was calculated from gross section properties. The Young's modulus of concrete, the cracking moment, M_c, and the yielding moment, M_y (taken equal to M_u; Table 3) were calculated according to the AIJ standards for structural calculations [27] (Appendix B). The post-cracking stiffness reduction factor, α, was also calculated using the AIJ standards [27], while the post-yielding hardening ratio, β, was set to 0.0025 uniformly across all members. The value for β was determined through trial-and-error analyses to produce the best match to experimental data. Wall CW2 was the only member to be modeled with strength degradation as it experienced shear failure during Run 5. The flexural spring strength for CW2 was modeled to rapidly decrease to zero following attainment of M_y. This approach was taken to reflect the low ductility in the CW2 wall, which had a shear margin ratio close 1.0, (shear margin ratio defined as the ratio of shear capacity Q_u to the shear demand at M_u, where inflection heights were based on preliminary modeling [32]). Nonlinear shear springs were also modeled for the CW1 and CW2 elements, where the cracking and yielding shear strength were defined using the AIJ standards [27] (Appendix B). The G1, G2 and G3 beam elastic properties and flexural spring parameters were modeled accounting for effective slab width (definition in Appendix B). Trial-and-error analyses showed that considering the full slab width effective in bending in both the X and Y-directions resulted in the best match to experimentally recorded lateral load capacity. Using the full slab width in strength calculation was not unexpected because the slab was constructed thicker than true $\frac{1}{4}$ scale, in order to meet strength requirements to support the added floor masses.

Time-history analyses of the structure were carried out using a single continuous acceleration record comprising the measured accelerations at the structure's foundation from Runs 1–9 in the X-direction and Runs 1–7 in the Y-direction. Though during the experiment both directions were loaded simultaneously, dynamic analysis was carried out in each direction independently. Lack of consideration for bi-directional loading

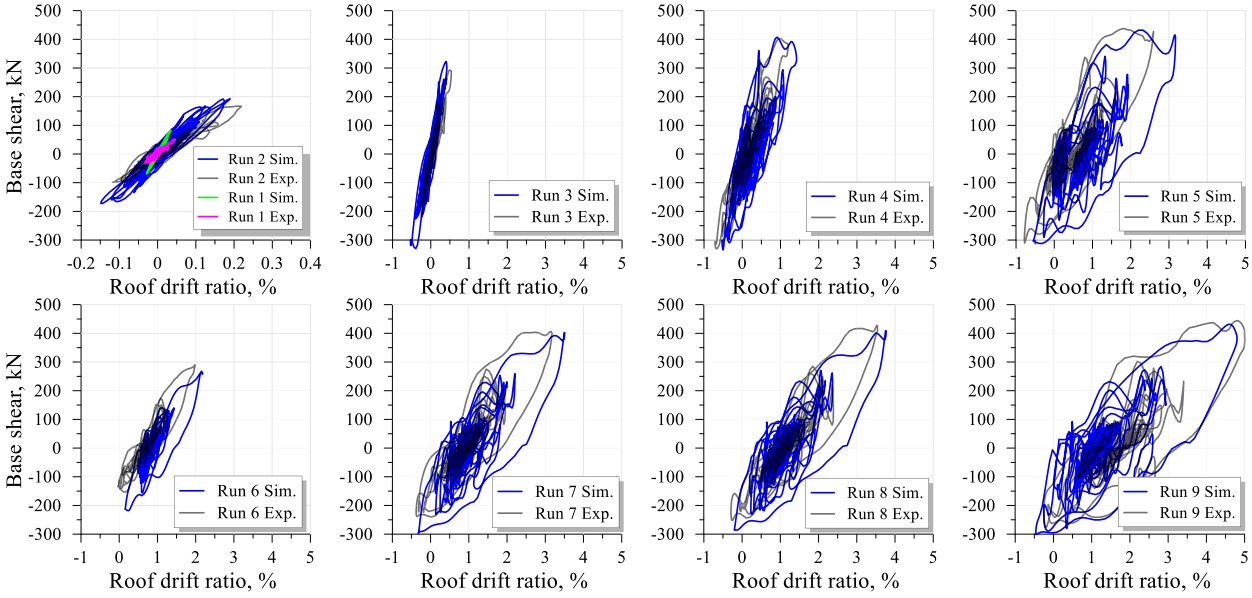

Fig. 12. Comparison of experimental and simulated base shear-roof drift ratio relationship in the X-direction.

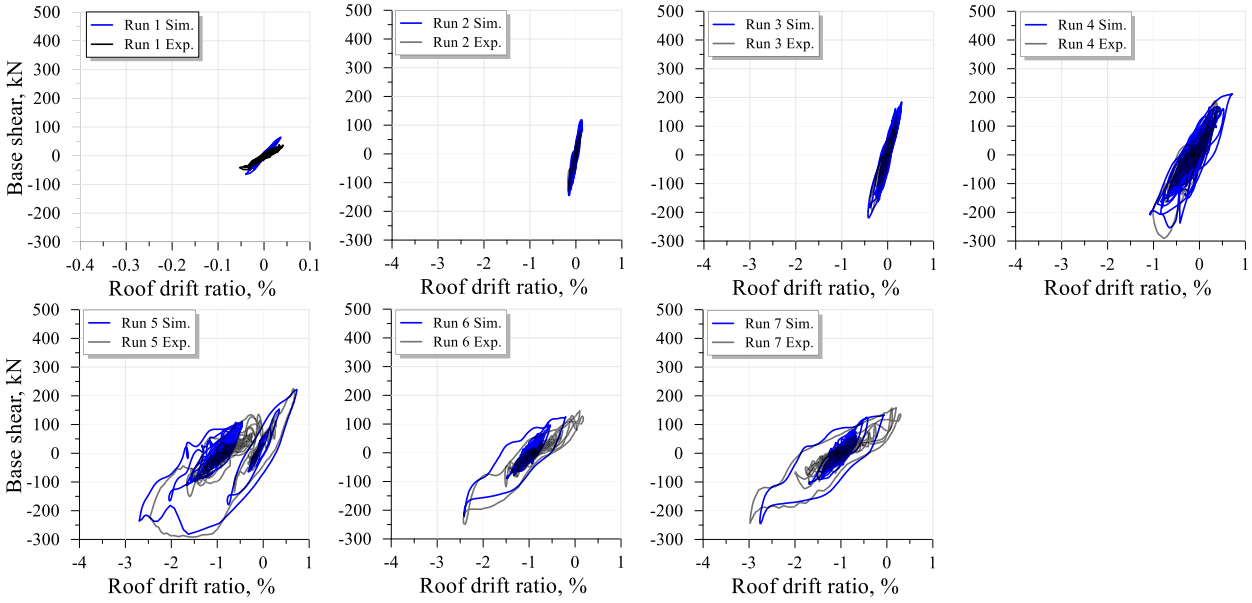

Fig. 13. Comparison of experimental and simulated base shear-roof drift ratio relationship in the Y-direction.

effects in the model were not expected to significantly affect the accuracy of the simulated results given the similarity of the experimental responses of Run 7 and 8 (where the only difference was the absence of the Y-direction loading component in Run 8). Findings from other shake table studies on RC frames have also shown an insignificant effect of bi-directional loading on the dynamic response characteristics [38]. The structure was given tangent-stiffness proportional damping of 3%. The Newmark algorithm ($\beta_{Newmark} = 0.25$) was used in the computation.

4.2. Model verification

Simulated base shear – roof drift ratio results are compared to the experimental data using overall response backbones shown previously in Fig. 9, and using hysteresis curves in Figs. 12 and 13 for the X and Y-directions, respectively. Though analyses were conducted using a combined continuous wave form of all Runs, the results of the analyses in Figs. 12 and 13 have been separated by Run for easier interpretation. A comparison of vertical distribution of maximum inter-story drift ratio is shown in Fig. 14. Initial stiffness is lower in the experiment compared to the model for both X and Y-directions and this is thought to be due to a presence of initial cracking formed in the structure during its curing and transportation to the testing facility. Apart from this, overall the numerical model is able to reproduce the continuous dynamic response of the experimental structure with good agreement. Some details of the comparison are highlighted next.

For the X-direction the simulated response for Runs 1–4 is generally in good agreement with experimental data, as show in Fig. 12. In Run 5 the simulated roof drift ratio is 22% higher than the experimental result. This is attributed to the fact that the hardening ratio ($\beta = 0.0025$) was assumed uniform for all members, whereas this value is likely higher in all walls due to a high longitudinal reinforcement ratio. Inter-story drift ratio distributions shown in Fig. 14a are generally consistent with the experimental data, except some overestimation of first story drifts from Run 5 onwards. This is thought to be due to the modeling of the wall plastic hinge at the base rather than some height above the foundation. Simulated responses of Run 6–9 are in good agreement with

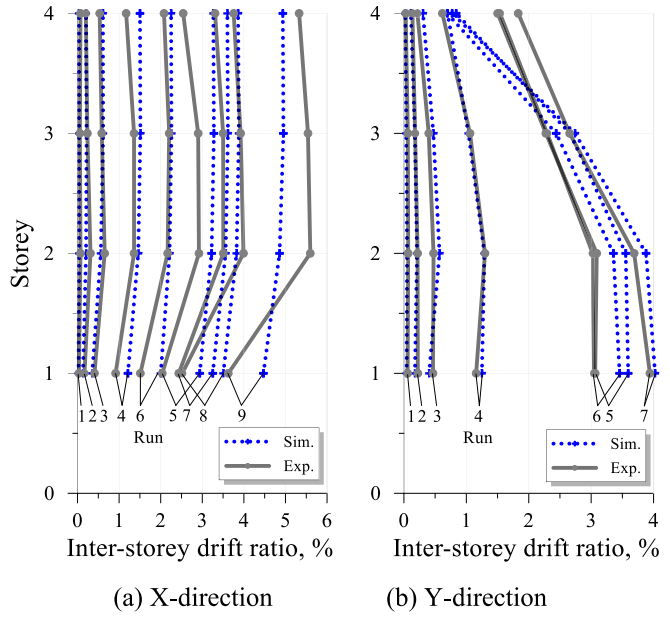

Fig. 14. Comparison of maximum inter-story drift ratio distribution between experiment and model.

experimental results when considering the follow-on effect of the imprecision encountered in the Run 5 simulation. Y-direction simulation results for all Runs shown in Fig. 13 are also in good agreement with the experimental data. In Fig. 14b it can be seen that there is a higher concentration of inter-story drift in the lower two stories in the simulated response compared to the measured response from Run 5 onwards. This is attributed to the rapid strength degradation set for the CW2 wall flexural spring, whereas in the experiment reinforcement dowel action likely provided appreciable residual strength and stiffness across the diagonal shear crack, which allowed a degree of force transmission to the upper stories. For additional verification, the story-shear – story drift ratio relationships were also examined and were found to produce a consistent level of agreement to the experimental data (full plots provided in Appendix C). Based on the above observations, though some structural intricacies are not perfectly reproduced in the modeling approach, the simulated global response is reasonably consistent with the experimental results. This model is thus deemed reliable for calculation of the 'benchmark' seismic residual capacity ratio at various damage states.

5. Determination of benchmark residual capacity ratio and comparison to approximate calculation methods

The model described in the previous section was used to determine the ground motion intensity required to reach the test structure's ultimate limit state from the undamaged state (${}_uS_a$) and from the damaged states following each Run (${}_dS_a^i$, where i is the Run number) via trial-and-error approach. For example, ${}_dS_a^i$ is the ground motion intensity required for the stucture to reach ultimate limit state directly following damage from Run 1. In this study, the 'ultimate limit state' of the structure is defined as the point at which any story reaches an inter-story drift ratio of 5%, a common limit used for gravity frames [39]. In the X-direction, as the maximum measured inter-story drift ratio of Run 9 exceeded 5% (Table 6), the maximum response of Run 9 is taken as the ultimate limit state (i.e., zero residual capacity). The 'benchmark' residual capacity ratio of the structure following each Run, R_b^i, was then computed using Eq. (1). The results of R_b^i are plotted against the maximum inter-story drift ratio of Run i in Fig. 15 (in the X-direction, R_b^i is only calculated until Run 8 as $R_b^9 = 0$). Residual capacity ratio calculations based on the JBPDA Guidelines (R_{IE}^i and R_{SIE}^i) were carried out using Eq. (2) and Eq. (3), where the η-factors were set based on the observed damage reported in Fig. 10. The results are plotted against the corresponding maximum inter-story drift ratio in Figs. 15a and 15b for the X-direction and Y-direction, respectively. To enable comparison to R_b^i, the approximate residual capacity ratio for Runs 7 and 8 (Runs with no damage inspection conducted) is linearly interpolated between Runs 6 and 9 and is distinguished by dashed lines in Fig. 15a. Boundaries for the overall building damage state as per the JBDPA Guidelines (see Appendix A) are indicated as grey dashed lines.

For both loading directions, R_b^i decreases gradually with respect to inter-story drift ratio as damage accumulates in the structure over the loading sequence. The final R_b^i determined for the X and Y-directions were R_b^8= 61% and R_b^7= 66%, respectively. Comparing to the approximate calculation methods in the elastic range of the structure (Run 1–3), both R_{IE}^i and R_{SIE}^i are consistent with each other and are within 5% of R_b^i for both the X and Y-directions. Good agreement to R_b^i is desirable in the elastic range to avoid unreasonably conservative retrofit or demolition decisions being made to otherwise essentially undamaged structures. Comparatively, after the structure enters the plastic region (Run 4 onwards) the approximate calculations provide an increasingly conservative estimate of R_b^i. This tendency is desirable as evaluation of the degree of ductility exerted in members is increasingly difficult to visually assess with certainty. Specific trends observed in each loading direction are discussed next.

In the X-direction, R_{IE}^i and R_{SIE}^i are calculated to be 50–60% less than R_b^i from Run 5 onwards. This large discrepancy is mainly attributed to an acute reduction of the damage η-factor for flexural walls from Damage Level III (η = 0.4; Table 2) to IV (η = 0.1; Table 2). The X-direction CW1 walls experienced significant spalling during Run 5, which exposed longitudinal reinforcement and thus incurred a Damage Level IV evaluation. As the CW1 walls provided a relatively high contribution to the overall lateral shear capacity of the test structure (~80% as measured from load cell data), the Damage Level IV evaluation induced a significant reduction in the residual capacity term in Eqs. (2) and (3). In reality, ductile walls subjected to low-moderate axial load typically maintain their flexural strength well beyond spalling damage, as exemplified by the CW1 walls not failing until Run 9 (as well as in numerous component-level studies [40–42]). Reduction of the level of conservativeness observed in Fig. 15a can be achieved by either increasing the Damage Level IV η-factor for flexural walls or revising the triggering criteria for a Damage Level IV assessment (for example requiring observations of bar buckling with limited concrete core damage). The similarity of the negative gradient of R_{IE}^i and R_{SIE}^i compared with R_b^i in Fig. 15a following Run 5 suggests that η-factors for beams and columns are suitably proportioned. Explicit consideration of different member deformation capacities in calculation of R_{IE}^i resulted in a 10–30% increase in the residual capacity ratio compared to if assuming equal deformation capacity in R_{SIE}^i. Thus, explicit consideration of deformation capacity will lead to residual capacity ratio estimates closer to R_b^i.

In the Y-direction the residual capacity ratio calculated via the approximate methods are consistent with each other and are 10–35% less than R_b^i, on average. Unlike the X-direction, the steep drop of approximate residual capacity ratio following shear failure of CW2 (Run 5) is not observed. This is because the η-factor reduction from Damage Level III (0.3; Table 2) to IV (0; Table 2) is a reasonable representation of the capacity reduction expected in a shear failure. Consideration of deformation capacity of members in calculation of R_{IE}^i resulted in an increase of residual capacity ratio of around 10%. This difference is lower than that observed for the X-direction because the contribution of the CW2 wall to the overall Y-direction lateral capacity is lower than the contribution of the two CW1 walls to the X-direction lateral capacity (from load cell data ~36% in the Y-direction vs ~80% in the X-direction). Therefore, the amount of wall to frame interaction plays a key role in the amount of conservativity the 'equal deformation capacity' assumption produces in the residual capacity ratio approximation. Though in both X and Y-directions R_{SIE}^i is more conservative than R_{IE}^i, the differ-

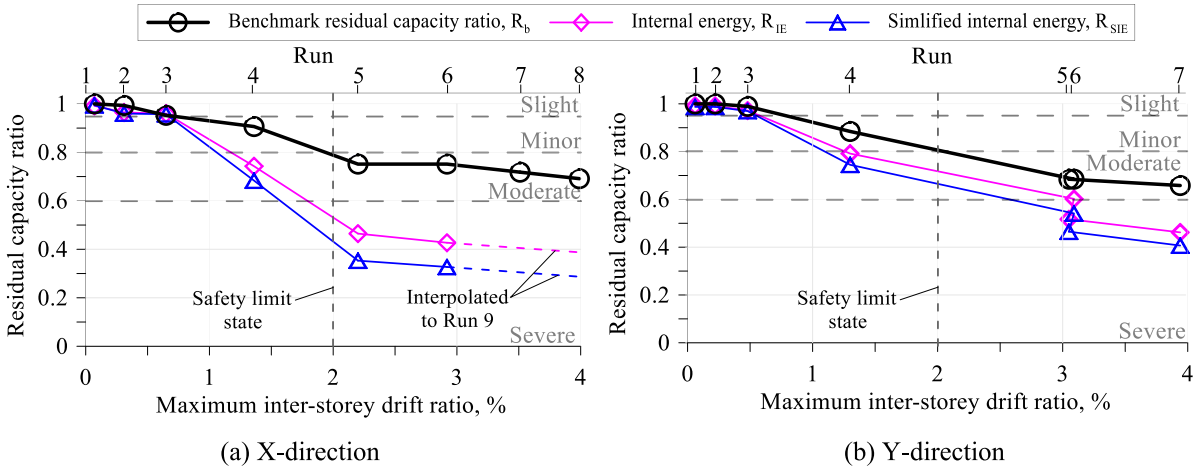

Fig. 15. Comparison of 'benchmark' and approximate seismic residual capacity ratio.

ence is not deemed significant and suggests that in a time-constrained damage assessment scenario assuming equal deformation capacity may not be unreasonable.

It is noted in Fig. 15 that R_b^i remains above 60% in both loading directions despite extensive damage throughout the structure, as opposed to gradually approaching zero as the structure nears collapse. An effective 'lower limit' to residual capacity such as this is not unreasonable considering that even a structure close to an 'ultimate limit state' would still possess an elastic region that would require a certain earthquake magnitude to overcome. The results from this single case study suggest that this limit is around R_b^i = 60%. This value corresponds to the boundary for 'Severe' damage in the JBDPA Guidelines, suggesting that a physical interpretation of the 'Severe' damage state is a structure that is at its ultimate limit state. Further numerical studies are needed to confirm whether the 60% limit holds for other building typologies and input ground motion characteristics.

6. Conclusion

To evaluate the approximate calculation methods of seismic residual capacity ratio in the JBDPA Guidelines, an experimental case study was conducted on a $\frac{1}{4}$ scale 4-storey RC structure via shake-table testing. It was shown in this study how an experimental value for residual capacity ratio, R_b, can be computed with the aid of a numerical model calibrated to the experimental results. Residual capacity ratio estimated from observed damage using the JBDPA Guidelines (R_{IE} and R_{SIE}) were then benchmarked against R_b. The following conclusions are drawn from this study.

(1) The safety limit state evaluation of the test structure using typical criteria in the AIJ standards was found to be generally conservative with respect to experimental data. The primary reasons for this being a low accuracy estimate of wall deformation capacity, and a lack of consideration for the relative contribution of the wall and frame to the overall structural capacity.
(2) R_b was shown to decrease gradually with respect to the maximum inter-story drift as damage accumulated in the structure. In both loading directions the lowest value of R_b reached prior to the ultimate limit state was close to 60%, suggesting that $R_b \leq 60\%$ represents a structure that is near or at its ultimate limit state.
(3) The assessment results of the approximate residual capacity ratio, R_{IE} and R_{SIE}, were generally consistent and accurate (within 5% of R_b) for the pre-yield region of the test structure's X and Y-directions.
(4) Following yield, R_{IE} and R_{SIE} for the X-direction were highly conservative (50–60% lower) with respect to R_b. This was judged to be due to the low value of the damage reduction η-factor of 0.1 applied to the X-direction CW1 walls once a Damage Level IV was reached. Thus, careful judgement should be exercised when assigning a level IV damage state to flexural walls to avoid an overly conservative assessment. An overly conservative evaluation was not observed for the Y-direction because the damage reduction η-factors used for the CW2 wall are consistent with the rapid decline of capacity associated with shear failure.
(5) Explicit consideration of deformation capacity resulted in 10–30% higher residual capacity ratio than if assuming all members have equal deformation capacity. While explicit consideration for deformation capacity can be used to obtain a higher accuracy of residual capacity ratio (particularly for cases where strong wall-frame interaction is expected), the equal deformation capacity assumption seems to be appropriate given time-constraints faced in damage evaluations.

While this study focused on rapid methods to evaluate residual capacity ratio, it is also of interest to understand the suitability other elaborate methods that require detailed numerical analysis studies [6,11,34,43]. Consideration of the accuracy of these relative to R_b is left as a subject of a future study.

Declaration of Competing Interest

The authors declare that they have no known competing financial interests or personal relationships that could have appeared to influence the work reported in this paper.

Acknowledgements

The research presented in this paper was jointly funded by Obayashi Corporation and the Consortium for Socio-functional Continuity Technology (http://www.softech.titech.ac.jp/; Project ID: JPMJOP1723 under Japan Science and Technology Agency). The authors would also like to express their gratitude to the technical staff at Obayashi Corporation and members of Maeda Lab who helped execute the experiment and perform damage observations of the structure.

Appendix A

The usability and repair decision matrix for damaged buildings available in the JBDPA Guidelines [14] is reproduced in Table A1. Decisions are based on the seismic residual capacity ratio, R, the intensity of the earthquake and the age of the building.

Table A.1
Building damage state classification based on *R* and the corresponding recovery decision.

Damage / Intensity*	Slight	Minor	Moderate	Severe/Collapse
	R ≥ 95%	80% ≤ R < 95%	60% ≤ R < 80%	R < 60%
5	×	×	×	×
6+	◎	○	△	△
6-	◎	○(△)†	△	△
6+	◎	◎(○)	○(△)	△

* Intensity scale is based on the Japanese Meteorological Agency earthquake magnitude scale.

† Brackets indicates the judgement pertaining to structures built before 1971.

◎ Light repairs are necessary. However, members damaged to Damage Level III or higher require structural repair measures)

○ Urgent structural repairs required to rehabilitated structure to pre-earthquake condition prior to use.

△ Urgent propping and repairs necessary. Building cannot be used until rehabilitation measures are implemented

× Detailed inspection following by assessment required using [44]

Appendix B. Strength and stiffness calculations based on the AIJ guidelines

The following provides a brief summary of the equations that were used to calculate the section strengths and stiffness reduction factors using the AIJ standards [26,27]. Notations used in the equations in this appendix are summarized in Table B1.

The following list of equations are with reference to parameters shown in the trilinear hinge model Fig. B1.

Flexural Cracking Strength, M_c

$$M_c = 0.56\sqrt{f'_c}Z + \mathrm{Nd}/6 \tag{B.1}$$

Flexural Strength, M_u

$$M_u = 0.8a_t\sigma_y d + 0.5\mathrm{N}d\left(1 - \frac{N}{bd\,f'_c}\right) \tag{B.2}$$

Stiffness Reduction Factor Post-yield

$$\alpha_y = \begin{cases} \left(0.043 + 1.64n\rho_t + \frac{0.043a}{D} + 0.33\eta_0\right)\left(\frac{jd}{D}\right)^2, & \frac{a}{D} \geq 2 \\ \left(-0.0836 + \frac{0.159a}{D} + 0.169\eta_0\right)\left(\frac{jd}{D}\right)^2, & \frac{a}{D} < 2 \end{cases} \tag{B.3}$$

$$\alpha = \frac{M_u - M_C}{\frac{M_u}{\alpha_y} - M_C} \tag{B.4}$$

Cracking Shear Strength, V_c

$$V_c = \phi\sqrt{\sigma_t^2 + \sigma_t\sigma_0}\mathrm{bd}\frac{1}{\kappa} \tag{B.5}$$

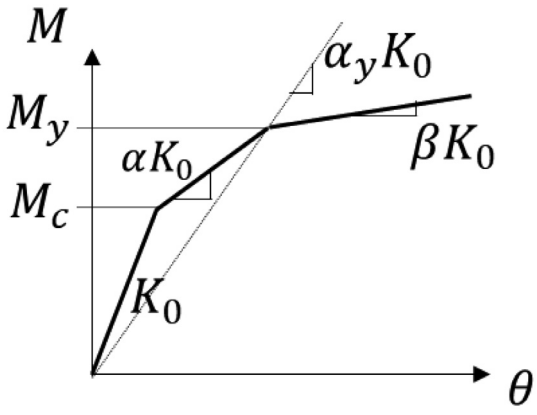

Fig. B1. Trilinear backbone parameter definitions used in modeling flexural springs.

Ultimate Shear Strength (Truss-Arch Theory), V_u

$$V_u = \min\begin{cases} \mu\rho_{we}\sigma_{wy}b_e j_e + \left(\nu f'_c - \frac{5\rho_{we}\sigma_{wy}}{\lambda}\right)\frac{bd}{2}\tan\theta_t \\ \frac{\lambda\nu f'_c + \rho_{we}\sigma_{wy}}{3}b_e j_e \\ \frac{\lambda\nu f'_c}{2}b_e j_e \end{cases} \tag{B.6}$$

Where,

$\mu = 2 - 20\theta_p$

$\nu = (1 - 20\theta_p)\nu_0$

$\nu_0 = 0.7 - \frac{f'_c}{200}$

$\lambda = 1 - \frac{s}{2j_e} - \frac{b_s}{4j_e}$

$b_s = \frac{b_e}{N_s + 1}$

Table B.1
Notation used.

Symbol	Unit	Explanation
a	mm	Shear span ratio of member
a_l	mm	Clear span length between adjacent beams
b	mm	Width of member
b_e	mm	Effective width of member measured to centers of outside legs of horizontal reinforcement
b_s	mm	Largest spacing between adjacent horizontal reinforcement legs in the member section
B	mm	Effective slab width
d	mm	Depth of member
E_c	MPa	Young's modulus of concrete
E_d	MPa	Dissipated energy
E_r	MPa	Remaining energy dissipation capacity
E_s	MPa	Young's modulus of reinforcement steel
f'_c	MPa	Compression strength of concrete
jd	mm	Effective member depth
je	mm	Effective depth of member measured to centers of outside legs of horizontal reinforcement
l	mm	Beam span length (measured to columns centers)
L	mm	Clear span length of member
M_c	Nmm	Cracking flexural capacity
M_u	Nmm	Ultimate flexural capacity (equal to yield flexural capacity, M_y, in a bilinear model)
M_y	Nmm	Yield flexural capacity (equal to ultimate flexural capacity, M_u,in a bilinear model)
n	–	Modular ratio of steel to concrete $=E_s/E_c$
N	N	Axial load
N_s		Number of horizontal reinforcement legs
s	mm	Spacing of horizontal reinforcement along the member longitudinal axis
V_c	N	Cracking shear strength
V_n	N	Nominal shear strength
V_u	N	Ultimate shear strength
Z	mm^3	Section modulus of member
α	–	Post-cracking flexural stiffness reduction factor
α_y	–	Secant stiffness reduction factor to the yielding moment, M_y
η_0	–	Axial load ratio, $= N/(bdf'_c)$
θ_p	rad	Member ultimate plastic rotation capacity
θ_t	rad	Angle of action of arch mechanism
κ	–	Section shape factor, =1.5
λ	–	Truss mechanism effective factor
μ	–	Compression truss angle factor, $= 2 - 20R_p$
ν	MPa	Concrete compression strength factor
ρ_t	–	Longitudinal tensile reinforcement ratio
ρ_{we}	–	Horizontal reinforcement ratio
σ_0	MPa	Gross section axial stress due to axial load
σ_t	MPa	Tensile strength of concrete, $= 0.33\sqrt{f'_c}$
σ_y	MPa	Tensile yield stress of longitudinal reinforcement
ϕ	–	Strength factor, = 0.51

$$\tan\theta_t = \begin{cases} \frac{0.9d}{2L}, & L/d \geq 1.5 \\ \frac{\sqrt{L^2+d^2}-L}{d^2}, & L/d < 1.5 \end{cases}$$

Ultimate Shear Strength (Arakawa 'Mean' Method), V_{su}

$$V_{su} = \left\{ \frac{0.068\rho_t^{0.23}\left(f'_c + 18\right)}{\sqrt{\frac{M}{Qd} + 0.12}} + 0.85\sqrt{\rho_{we}\sigma_{wy}} + 0.12\sigma_0 \right\} b_e j \quad \text{(B.7)}$$

Where, $\frac{M}{Qd}$ is the shear span ratio and is no lesser than 1 and no greater than 3 at ultimate moment capacity state.

Effective Slab Width

The following equations are with reference to parameters defined in Fig. B2. Note that according to the below definitions maximum effective slab width should not exceed $a/2$.

$$B = \begin{cases} b + 2b_a, & for\ internal\ beams \\ b + b_a, & for\ external\ beams \end{cases} \quad \text{(B.8)}$$

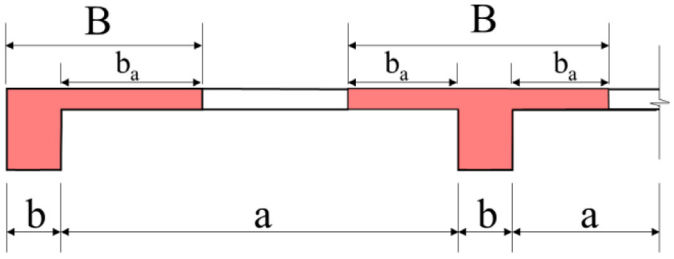

Fig. B2. Effective slab width definitions.

Where,

$$b_a = \begin{cases} \left\{0.5 - \left(\frac{0.6a}{l}\right)\right\}a, & \frac{a}{l} < 0.5 \\ 0.1l, & \frac{a}{l} > 0.5 \end{cases}$$

Appendix C. Simulated story shear – inter-story drift ratio results

The simluated story shear vs inter-story drift ratio relatinships are shown in Figs. C1 and C2 for the X-direction and Y-direction, respectively.

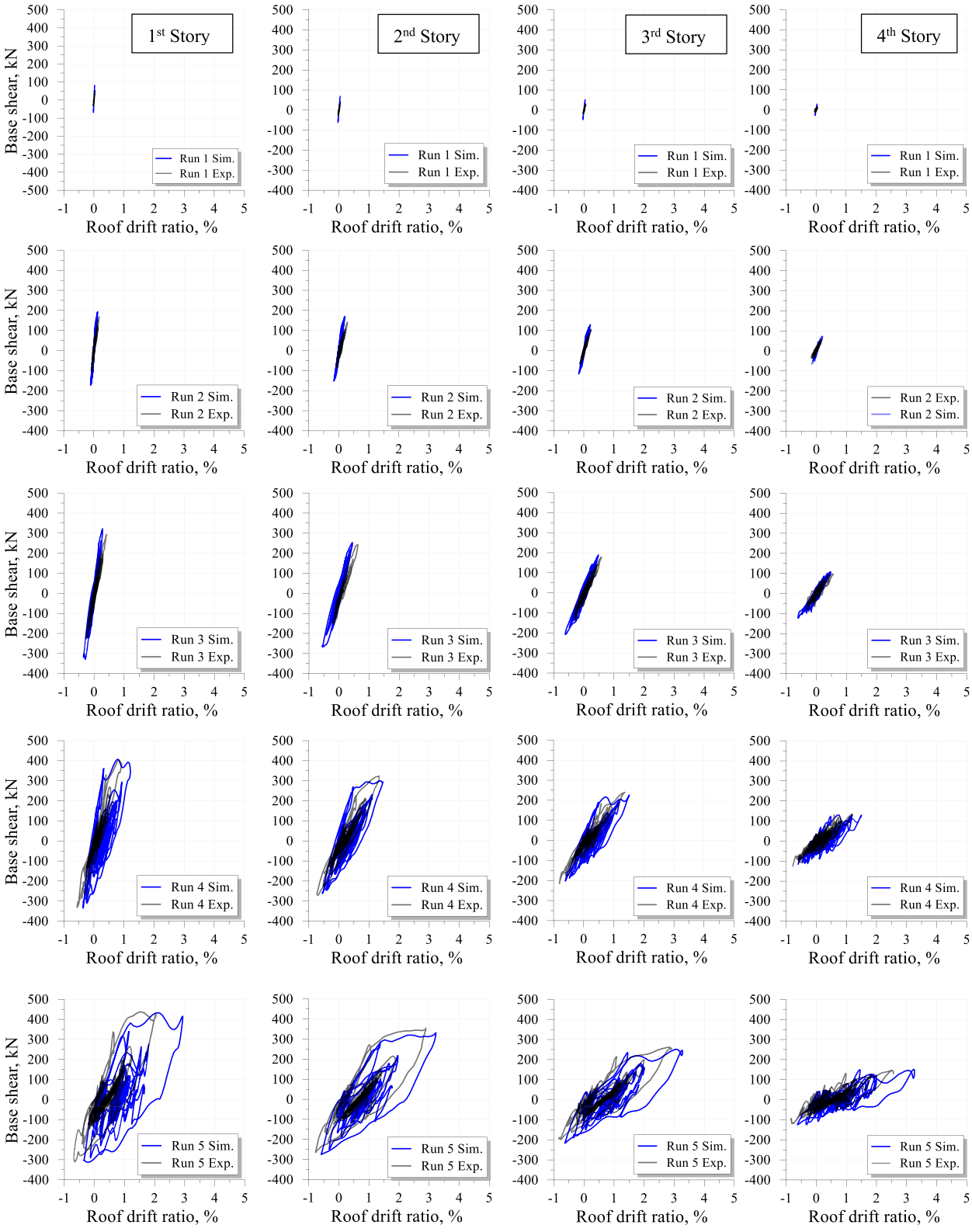

Fig. C1. Comparison of simulated vs experimental story shear – inter-story drift ratio results (X-direction).

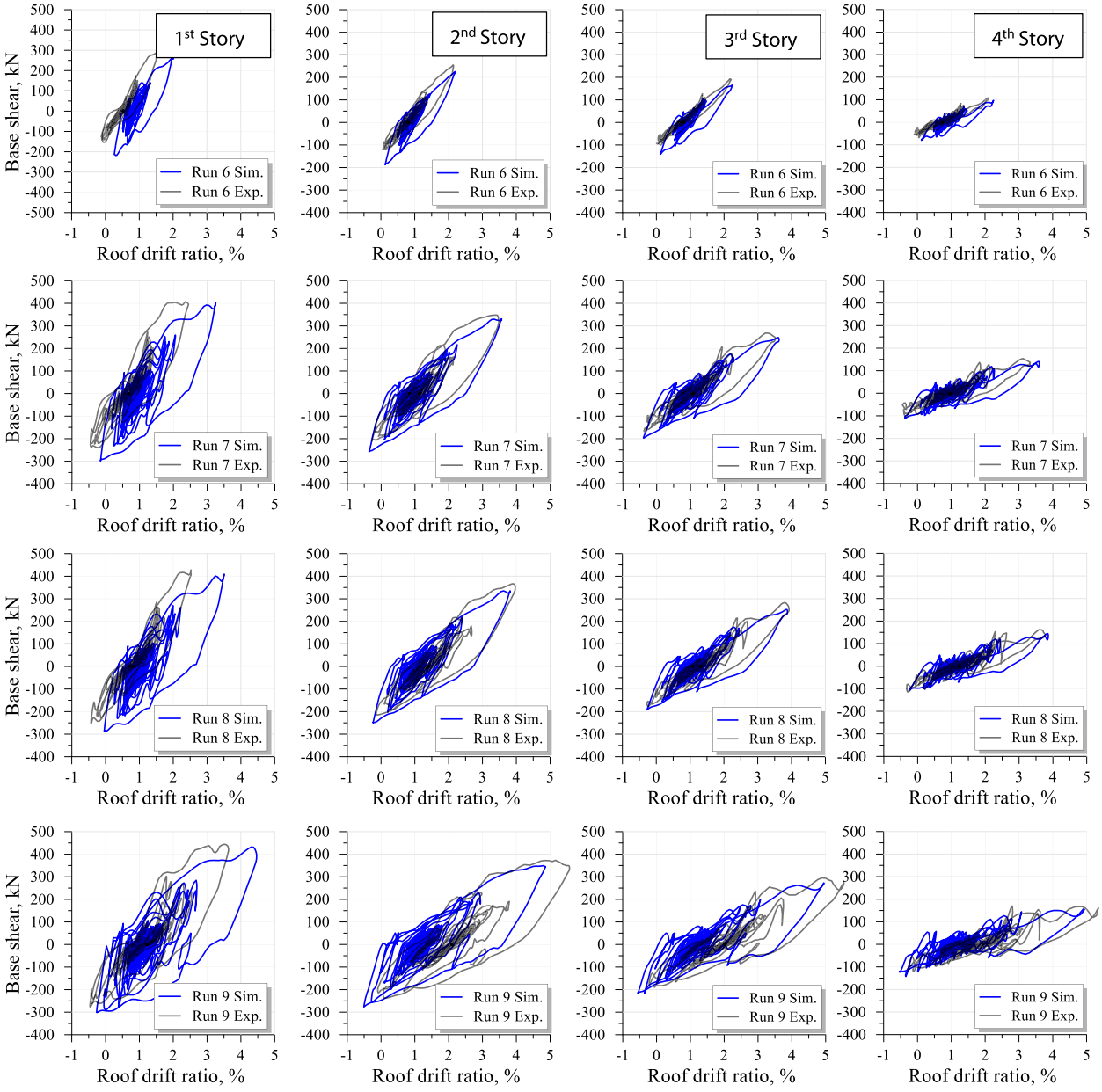

Fig. C1. Continued

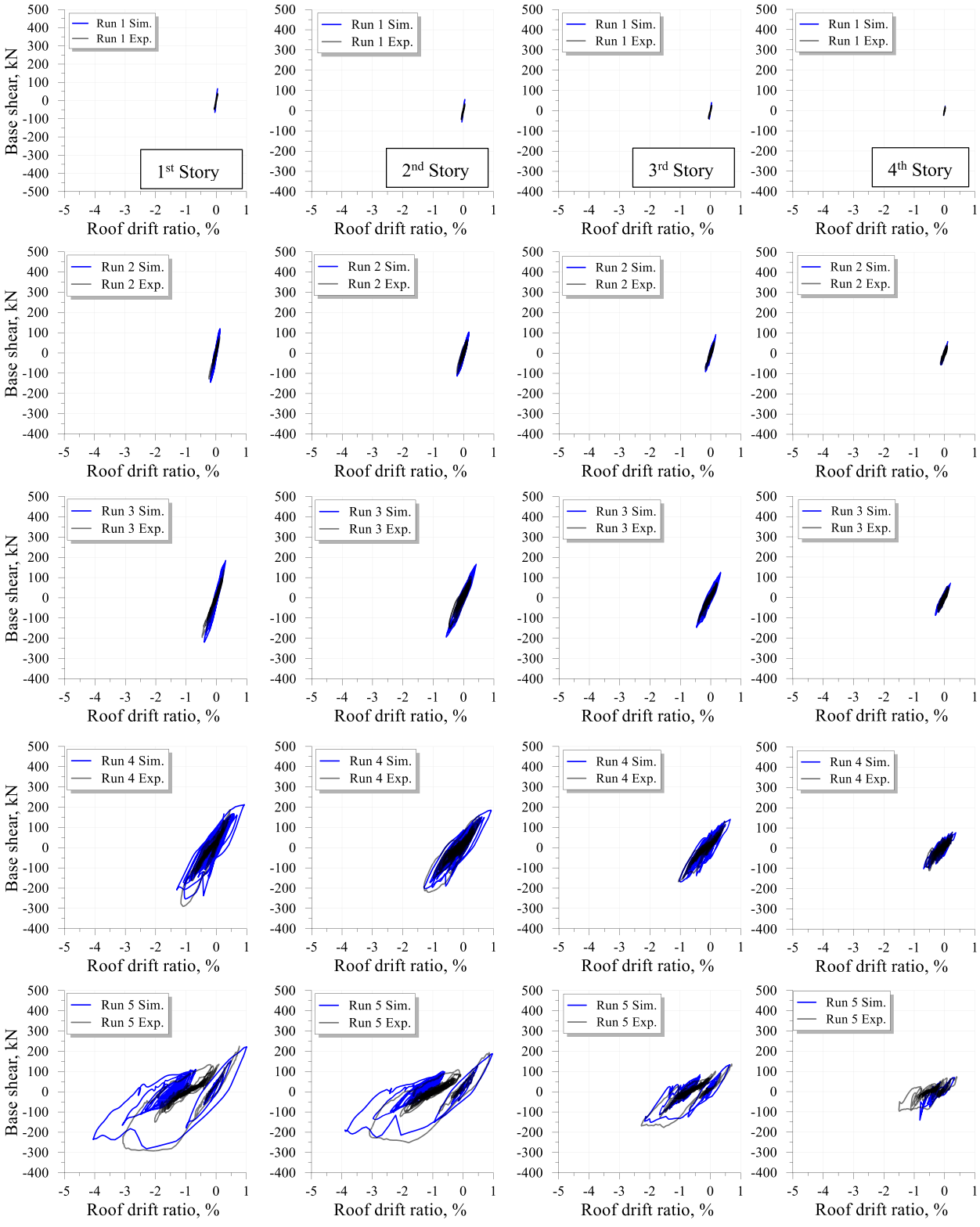

Fig. C2. Comparison of simulated vs experimental story shear – inter-story drift ratio results (Y-direction).

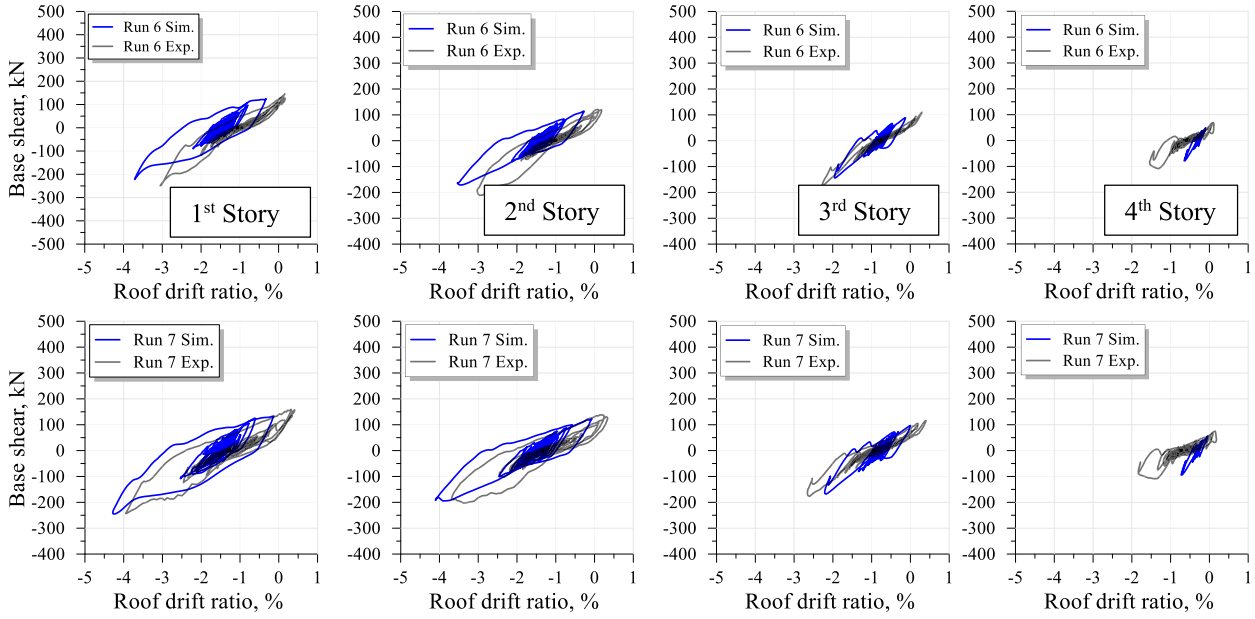

Fig. C2. Continued

References

[1] Nojavan A. Performance of full-scale reinforced concrete columns subjected to extreme earthquake loading. University of Minnesota; 2015. Ph.D thesis.

[2] Kawashima KK, Koyama T. Effect of number of loading of cycles reinforced columns on dynamic characteristics concrete. Struct Eng Earthq Eng 1988;5(1):183–91.

[3] Marder KJ, Motter CJ, Elwood KJ, Clifton GC. Effects of variation in loading protocol on the strength and deformation capacity of ductile reinforced concrete beams. Earthq Eng Struct Dyn 2018;47(11):2195–213. doi:10.1002/eqe.3064.

[4] Sarrafzadeh M. Residual capacity and repairability of moderately-damaged ductile reinforced concrete ductile frame structures. The University of Auckland; 2021. Ph.D thesis.

[5] Alwashali H, Maeda M, Ogata Y, Aizawa N, Tsurugai K. Residual seismic performance of damaged reinforced concrete walls. Eng Struct 2021;243(January):112673. doi:10.1016/j.engstruct.2021.112673.

[6] Ito T, Suzuki Y, Maeda M. Evaluation of residual seismic capacity of damaged RC buildings based on deterioration of strength, deformation and damping performance of damaged members (in Japanese). Proc Jpn Concr Inst Conf 2015;37(2):787–92.

[7] FEMA 307 Evaluation of earthquake damaged concrete and masonry wall buildings. Redwood City, CA: Federal Emergency Management Agency; 1998.

[8] Di Ludovico M, Polese M, Gaetani d'Aragona M, Prota A, Manfredi G. A proposal for plastic hinges modification factors for damaged RC columns. Eng Struct 2013;51:99–112. doi:10.1016/j.engstruct.2013.01.009.

[9] Chiu CK, Sung HF, Chi KN, Hsiao FP. Experimental quantification on the residual seismic capacity of damaged RC column members. Int J Concr Struct Mater 2019;13(1):3–22. doi:10.1186/s40069-019-0338-z.

[10] Chiu CK, Sung HF, Chiou TC. Post-earthquake preliminary seismic assessment method for low-rise RC buildings in Taiwan. J Build Eng 2022;46:103709. doi:10.1016/j.jobe.2021.103709.

[11] FEMA 306. Evaluation of earthquake damaged concrete and masonry wall buildings, basic procedures manual. Redwood City, CA: Federal Emergency Management Agency; 1998.

[12] Kusunoki K, Hinata D, Hattori Y, Tasai A. A new method for evaluating the real-time residual seismic capacity of existing structures using accelerometers: structures with multiple degrees of freedom. Jpn Archit Rev 2018;1(1):77–86. doi:10.1002/2475-8876.1010.

[13] Kusunoki K. Experimental study on the damage classification method with the performance curves of R\C structures derived from recorded accelerations. J Struct Constr Eng 2020;85(774):1055–65. doi:10.3130/aijs.85.1055.

[14] Japan Building Disaster Prevention Association Guidelines for post-earthquake damage evaluation and rehabilitation of RC buildings (in Japanese). Tokyo, Japan: Japan Building Disaster Prevention Association; 2015.

[15] Ministry of Business Innovation and Employment Field guide: rapid post disaster building usability assessment - earthquakes. Wellington, New Zealand: Ministry of Business Innovation and Employment; 2014.

[16] Applied Technology Council Procedures for postearthquake safety evaluation of buildings (ATC-20). Redwood City, California: Applied Technology Council; 1989.

[17] National Center for Research on Earthquake Engineering (NCREE) Technology handbook for seismic evaluation and retrofit of school buildings. 2nd ed. National Center for Research on Earthquake Engineering (NCREE); 2009. doi:10.1111/j.1949-8594.1962.tb08661.x.

[18] Baggio C, Bernardini A, Colozza R, Corazza L, Della Bella M, Di Pasquale G, et al. Field manual for post-earthquake damage and safety assessment and short term countermeasures (AeDES), Ispra, Italy: Reseach Center; 2007. EUR 22868 EN - 2007.

[19] Maeda M, Matsukawa K, Ito Y. Revision of guideline for post-earthquake damage evaluation of RC buildings In Japan. In: Proceedings of the NCEE 10th US national conference on earthquake engineering: frontiers of earthquake engineering; 2014.

[20] Maeda M, Al-Washali H, Matsukawa K. An overview of post earthquake damage and residual capacity evaluation for reinforced concrete buildings in Japan. In: Proceedings of the 7th international conference on computational methods in structural dynamics and earthquake engineering methods in structural dynamics and earthquake engineering; 2019. p. 930–43. doi:10.7712/120119.6969.19228.

[21] Maeda M, Honda Y, Kang D. Post-earthquake damage level and repair cost for reinforced concrete school buildings. In: Proceedings of the 11th Japanese association of earthquake engineering symposium. Japanese Association of Earthquake Engineering; 2002.

[22] Maeda M, Nakano Y, Lee KS. Post-earthquake damage evaluation for R/C buildings. In: Proceedings of the council on tall buildings and urban habitat, Seoul, Korea; 2004. Ocober 10-13.

[23] Polese M, Di Ludovico M, Marcolini M, Prota A, Manfredi G. Assessing repairability: simple tools for estimation of costs and performance loss of earthquake damaged reinforced concrete buildings. Earthquake Eng Struct Dyn 2015;44:1539–57. doi:10.1002/eqe.

[24] Nakano Y, Maeda M, Kuramoto H, Murakami M. Guideline for post-earthquake damage evaluation and rehabilitation of RC buildings in Japan. In: Proceedings of the 13th world conference on earthquake engineering; 2004.

[25] Building Center of Japan The building standard law of Japan. Tokyo, Japan: Building Center of Japan; 2016.

[26] Architectural Institute of Japan Design guidelines for earthquake resistant reinforced concrete buildings based on inelastic displacement concept. Tokyo, Japan: Architectural Institute of Japan; 1999.

[27] AIJ standard for structural calculation of reinforced concrete structures (in Japanese). Tokyo, Japan: Architectural Institute of Japan; 2018.

[28] Otani S, Sozen MA. Behavior of Multistory Reinforced Concrete Frames During Earthquakes. Structural Research Series No. 392, University of Illinois, Urbana; 1972.

[29] Laughery L. Response of high-strength reinforced concrete structures to simulated earthquakes. Purdue University; 2016. Ph.D thesis.

[30] Cecen H. Response of ten storey, reinforced concrete model frames to simulated earthquakes. University of Illinois at Urbana-Champaign; 1979. Ph.D thesis.

[31] Shegay AV, Miura K, Akira M, Maeda M, Seki M. Performance recovery of a repaired 4-storey reinforced concrete structure subjected to shake-table testing. Earthquake Eng Struct Dyn 2023:1–21. doi:10.1002/eqe.3818.

[32] Miura K, Fujita K, Tabata Y, Maeda M, Shegay A, Yonezawa K. Shake-table test of a 4-storey frame-wall RC strcture to investigate the collapse mechanism and safety limit (in Japanese). J Struct Constr Eng 2021;86(780):247–57. doi:10.3130/aijs.86.247.

[33] Maeda M, Kang DE. Post-earthquake damage evaluation of reinforced concrete buildings. J Adv Concr Technol 2009;7(3):327–35. doi:10.3151/jact.7.327.

[34] Fujita K, Miura K, Tabata Y, Maeda M, Shegay AV, Seki M. Post-earthquake capacity evaluation of RC frame structures with multi-story flexural walls (in Japanese). J Struct Constr Eng 2021;86(785):1084–94. doi:10.3130/aijs.86.1084.

[35] Kozo Systems Corporation Stuructral nonlinear analysis program (SNAP) ver.7. Kozo Systems Corporation; 2019.

[36] Takeda T, Sozen MA, Nielsen NN. Reinforced concrete response to simulated earthquakes. J Struct Div 1970;96(12):2557–73. doi:10.1061/JSDEAG.0002765.
[37] Tripathi M, Dhakal RP, Dashti F, Massone LM. Low-cycle fatigue behaviour of reinforcing bars including the effect of inelastic buckling. Constr Build Mater 2018;190:1226–35. doi:10.1016/j.conbuildmat.2018.09.192.
[38] Hagiwara H, Nakayama T, Igarashi K. Bidirectional shaking table tests of a one–fourth scale reinforced concrete space frame. In: Proceedings of the 12th World Conference on Earthquake Engineering, Auckland, New Zealand; 2000. Paper No. 0645.
[39] FEMA P-2012 Assessing seismic performance of buildings with configuration irregularities. Redwood City, CA: Federal Emergency Management Agency; 2018.
[40] Shegay AV, Motter CJ, Elwood KJ, Henry RS, Lehman DE, Lowes LN. Impact of axial load on the seismic response of rectangular walls. J Struct Eng 2018;144(8):1–32. doi:10.1061/(ASCE)ST.1943-541X.0002122.
[41] Segura CL Jr, Wallace JW. Seismic performance limitations and detailing of slender reinforced concrete walls. ACI Struct J 2018;115(3):849–59. doi:10.14359/51701918.
[42] Lu Y, Gultom RJ, Ma QQ, Henry RS. Experimental validation of minimum vertical reinforcement requirements for ductile concrete walls. ACI Struct J 2018;115(4):1115–30. doi:10.14359/51702048.
[43] Miura K, Maeda M. Evaluation method of contribution factor of structural components for seismic capacity assuming invariable inter-story drift before and after damaged and investigation of applicability to RC frames with beam yielding mechanism (in Japanese). J Struct Constr Eng 2018;83(747):727–37. doi:10.3130/aijs.83.727.
[44] The Japan Building Disaster Prevention Association Standard for seismic evaluation of existing reinforced concrete buildings (in Japanese). Tokyo, Japan: The Japan Building Disaster Prevention Association; 2001.